

# 9 Photoacoustic and Thermoacoustic Tomography: Consistency Conditions and the Partial Scan Problem

Sarah K. Patch  
University of Wisconsin-Milwaukee

## CONTENTS

9.1 Introduction .....	103
9.1.1 Mathematical Model .....	103
9.1.2 Background: Inversion Formulae .....	104
9.1.3 Background: Uniqueness, Invertibility, Consistency Conditions .....	105
9.1.4 Limited Angle Reconstruction .....	105
9.2 Theory: Consistency Conditions on Measured Pressures .....	106
9.3 Application: Consistency Conditions on Measured Pressures .....	107
9.4 Numerical Methods .....	108
9.4.1 Computing Moments, $c_k(\mathbf{x})$ .....	109
9.4.2 Computing Coefficients $d_k^l(\Phi)$ .....	110
9.4.3 Estimating Unmeasured Pressures $p(x_3, \phi, t)$ : Stability and Computational Cost .....	110
9.4.3.1 Stability .....	110
9.4.3.2 Computational Cost .....	111
9.5 Numerical Results .....	111
9.6 Conclusions .....	112
References .....	112

## 9.1 INTRODUCTION

This article is motivated by application of thermo/photoacoustic tomography to mammography. Early experimental work generated impressive reconstructions despite several simplifying assumptions about the physics of acoustic wave propagation and detection with standard ultrasound transducers [1–10]. Idealized thermo- and photoacoustic data represent spherical integrals, and reconstruction requires inverting the spherical Radon transform. Therefore, we use the acronym TCT for thermoacoustic computerized tomography, to emphasize similarities with inversion of the standard Radon transform in x-ray computerized tomography (CT).

A clinically unrealizable assumption is that transducers may be placed at any point on a surface that completely encloses the object. Clinically realizable mammography data sets will permit roughly one-half of the desired measurements because transducers may be placed only on the lower hemisphere of a tank in which the breast is immersed, as depicted in Figure 9.1. This deficiency is typically ignored, by simply zero-filling missing measurements. A computationally efficient method for extending incomplete data sets so that they obey a necessary and sufficient subset [11] of the consistency conditions upon idealized TCT data was derived

in Ref. [12]. We validate these theoretical results numerically, demonstrating that enforcing consistency conditions can reduce low-frequency errors in reconstructions of zero-filled partial-scan data. This permits tighter windowing of displayed images, improving visibility of low-contrast inclusions that are washed out by a large display window.

### 9.1.1 MATHEMATICAL MODEL

Pressures generated by TCT excitation are governed by the inhomogeneous wave equation with separable source term and homogeneous initial conditions [13]

$$\frac{1}{v_s^2} \frac{\partial^2}{\partial t^2} p(\mathbf{x}, t) - \Delta_{\mathbf{x}} p(\mathbf{x}, t) = \frac{\beta}{C_p} A_e(\mathbf{x}) \frac{\partial}{\partial t} A_t(t), \quad (9.1)$$

where  $\beta$  is the thermal expansion coefficient (in  $\text{K}^{-1}$ ),  $C_p$  is the specific heat capacity at constant pressure (in units of  $\text{J}/\text{kg}/\text{K}$ ) and  $v_s$  is the speed of sound (in  $\text{m}/\text{sec}$ );  $A_e(\mathbf{x})$  is the specific energy absorption at point  $\mathbf{x}$  (in  $\text{J}/\text{m}^3/\text{sec}$ ), and the dimensionless function  $A_t(t)$  gives the temporal shape of the pulse. This model neglects several physical nonidealities, such as acoustic attenuation and nonconstant propagation speed,  $v_s = v_s(\mathbf{x})$ , etc. For simplicity, we rescale, setting  $v_s \equiv 1 \equiv \beta/C_p$ . Photoacoustic

what I am to verify??  
Please note that circled "x" should be boldface.  
AU: Please verify.

if possible modify to include:  
 $\nu_s = \nu_s(\mathbf{x})$ ,  
 $C_p = C_p(\mathbf{x})$ ,  $\beta = \beta(\mathbf{x})$ , etc

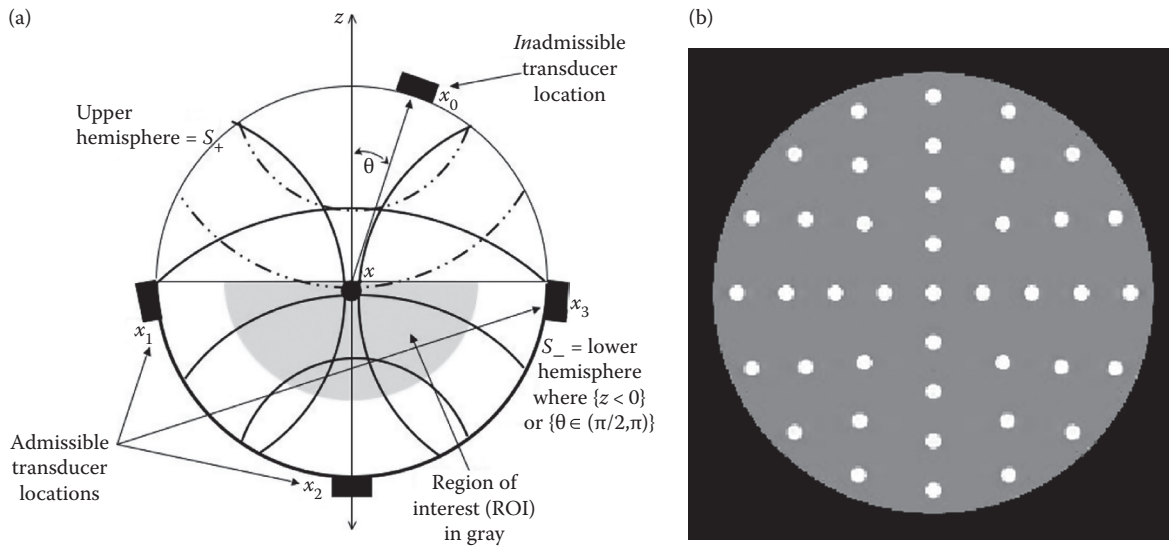


**FIGURE 9.1** The breast is immersed in a tank of water and transducers surround the exterior of the tank,  $S_-$ . Integrals of the RF absorption coefficient over spheres centered at each transducer are measured. Only “partial-scan” data may be measured, as we cannot put transducers on  $S_+$ .

excitation pulses are often approximated as  $A_e(t) = \delta(t)$  functions, resulting in solutions for  $p$  related to integrals of the heating function,  $A_e$ , over spheres, as depicted in Figure 9.1a

$$p(\mathbf{x}, t) = \frac{\partial}{\partial t} \left( \frac{1}{t} \int_{|\mathbf{y}-\mathbf{x}|=t} A_e(\mathbf{y}) d\mathbf{y} \right) \equiv \frac{\partial}{\partial t} \left( \frac{1}{t} R_{\text{TCT}} A_e(\mathbf{x}, t) \right). \quad (9.2)$$

The inversion problem is to recover the absorptivity function,  $A_e(\mathbf{x})$ , from measured data,  $p(\mathbf{x}, t)$ , where  $\mathbf{x}$  lies on a two-dimensional surface,  $S$ , surrounding the object. This implies that  $A_e$  is supported inside  $S$ . For the purposes of this paper, we assume  $A_e \geq 0$  and take a spherical measurement aperture,  $S = S^2 = \{\mathbf{x} \mid \|\mathbf{x}\| = 1\}$  parametrized with the standard  $(\theta, \phi)$ , so that  $\mathbf{x} \in S$  implies

$$\mathbf{x} = \begin{pmatrix} \sin \theta \cos \phi \\ \sin \theta \sin \phi \\ \cos \theta \end{pmatrix}$$

for  $\theta \in [0, \pi]$  and  $\phi \in [0, 2\pi)$ . We use the filtered backprojection (FBP) inversion as derived in Ref. [14] to reconstruct at points  $\|\mathbf{x}\| < 1$

$$A_e(\mathbf{x}) = \frac{-1}{8\pi^2} \int_{\mathbf{o} \in S} \frac{1}{t} \frac{\partial}{\partial t} (t^2 p(\mathbf{o}, t)) \Big|_{t=|\mathbf{x}-\mathbf{o}|} d\mathbf{o} \quad (9.3)$$

$$\textcircled{d\mathbf{o}} = \frac{-1}{8\pi^2} \int_{\mathbf{o} \in S} \frac{R''_{\text{TCT}} A_e(\mathbf{o}, |\mathbf{x}-\mathbf{o}|)}{|\mathbf{x}-\mathbf{o}|} d\mathbf{o}.$$

Application of thermoacoustics to breast imaging requires reconstructing at all points  $\mathbf{x}$  below the equatorial plane. Fortunately, inversion Formula 9.3 weights data from admissible transducer locations on  $S_-$  more heavily than data from  $S_+$  for reconstruction points  $\mathbf{x}$  below the equatorial plane.

Numerical validation of TCT image reconstruction via FBP as in Ref. [15] is used to generate the results presented below.

### 9.1.2 BACKGROUND: INVERSION FORMULAE

Background material on this spherical Radon transform can be found in the texts [16–18], as well as recent review articles [19,20]. The first inversion formulae for  $R_{\text{TCT}}$  were derived for planar [21], cylindrical, and spherical measurement apertures. Note that these geometries correspond to isosurfaces of orthogonal coordinate systems for which the Laplacian is separable. Infinite series solutions were derived in the early 1980s for spherical measurement apertures in two and three dimensions [22,23]. These solutions echo those found by Cormack for standard x-ray CT [24,25]. Inversion formulae of both FBP and  $\rho$ -filtered type were derived in Ref. [14] for odd-dimensions,  $n \geq 3$ . A formula of backprojection-filter type was derived in Ref. [26]. Recently, inversion formulae of FBP type were announced for even dimensions [27]. An FBP inversion that holds for any dimension is derived in Ref. [28]; a computationally efficient implementation is demonstrated in Ref. [29]. Sophisticated mollification of the high-pass filter in FBP reconstruction is presented in Refs. [30–32]. All of these results hold only for a spherical measurement aperture, but Kunyansky recently derived a mathematically exact series solution for nearly general measurement surfaces [28]. Like their counterparts in x-ray CT, these reconstructions are relatively stable. Unlike x-ray CT, however, TCT reconstruction is inherently three dimensional, and therefore easily localized to regions of interest (ROIs). Several photoacoustic laboratories are revisiting ultrasound detection methods that may impact the data model in Equation 9.2 [33–47]. For example, Finch and Rakesh reconstruct from the normal component of measured pressures in Ref. [19], largely accounting for anisotropic sensitivity of flat piezoelectric transducers.

AU: Too large to set on a text line. Is it ok to display?

It is OK

this equation is messed up if you cannot fit on a single line, please put the first d {mathbf{o}} back at the end of the first line and then align at the "=" sign

**9.1.3 BACKGROUND: UNIQUENESS, INVERTIBILITY, CONSISTENCY CONDITIONS**

A plethora of mathematical results on invertibility of spherical Radon transforms and thermoacoustic pressures exist; only a brief overview follows. Injectivity sets are those on which identically zero measurements imply an identically zero imaging object—and therefore unique reconstruction of nonzero data. Injectivity sets for two-dimensional  $R_{TCT}$  data are characterized in Ref. [48]; for a thorough survey of injectivity  $R_{TCT}$  in the plane see Ref. [49]. Injectivity in higher dimensions is discussed in Ref. [50].

The thermo- and photoacoustic effects map electromagnetic (EM) absorptivity functions  $A_e$  to measured pressures, or equivalently spherical integrals of  $A_e$ .

$$TCT: A_e(\mathbf{x}) \rightarrow p(\mathbf{x}, t). \tag{9.4}$$

The TCT map takes a function  $A_e(\mathbf{x})$  defined on  $\mathbf{x} \in \mathbf{R}^3$  to a function  $p(\mathbf{x}, t)$  defined on  $(\mathbf{x}, t) \in \mathbf{R}^3 \times \mathbf{R}^+$ . Clearly, the fact that the TCT map takes a function of three variables to a function of four variables implies the existence of very strong consistency conditions upon measured pressures. The strongest consistency condition is the *differential* condition imposed by the acoustic wave Equation 9.1, which reduces the number of *independent* variables upon which  $p$  is a function. Knowledge of  $p$  on suitable three-dimensional manifolds in  $\mathbf{R}^3 \times \mathbf{R}^+$  permits one to compute  $p$  in a four-dimensional volume bounded by the manifold by solving Equation 9.1. The *domain* of the TCT map is the class of all physically feasible—or consistent—functions,  $A_e(\mathbf{x})$ ; the *range* contains all physically feasible measurements,  $p(\mathbf{x}, t)$ . Characterization of the range is important because the range of a forward map is the domain of its inverse map. Consistency conditions upon measured data are often called range conditions in the mathematical literature. The range has recently been completely characterized for measurements restricted to the sphere in two space dimensions [51]; in odd space dimensions  $n=3,5,7, \dots$  [52]; and also arbitrary dimensions [11].

The differential condition 9.1 implies that  $p(\mathbf{x}, t)$  is closely related to spherical integrals of  $A_e$  in Equation 9.2, and this relationship can be inverted by the FBP Formula 9.3. Although integral conditions are weaker than differential conditions, they can be used to improve image quality (IQ). In x-ray CT, moment conditions may be used to detect faulty detector channels [53]. Below, we enforce some (but not all) of the integral consistency conditions to estimate data that cannot be measured by a clinical TCT breast imaging system, as depicted in Figure 9.1

**9.1.4 LIMITED ANGLE RECONSTRUCTION**

Mathematical results on tomographic inversion of partial-scan data typically focus on the ability to recover “singularities”, i.e., *edges* in the image. However, clinical imaging systems measure band-limited and discretely sampled data sets, from which *true* singularities cannot be recovered.

Nevertheless, large gradients in reconstructed images, visually perceived as jumps or interfaces, can be recovered and provide diagnostic value. We therefore give a brief (and by no means complete) review of limited angle reconstruction results. The “audible zone” of an object from a partial-scan data set refers to recoverable features [54] and is a particularly apt term for thermoacoustic tomography! Reconstruction of limited angle data is highly unstable outside of the “audible zone” for both standard x-ray CT [54–56] and spherical means, as measured in TCT [57] and SONAR [58]. Iterative reconstructions have already demonstrated that good IQ can be attained within the audible zone [57,59–63], but at prohibitively high computational cost. A FBP method was used for the two-dimensional problem in Ref. [64]. We corroborate these iterative results, improving reconstruction of zero-filled data with a computationally cheap two-step direct method:

1. Complete partial-scan data sets by enforcing low frequency consistency conditions on idealized TCT data.
2. Reconstruct complete data set.

This direct method is not a panacea, but can quickly create the initial image for updating via standard iterative methods. The phantom used to demonstrate our method (Figure ??) consists of a large sphere centered at the origin in which  $A_e=1$  with low-contrast spherical inclusions, as described in Table 9.1. For fixed  $\phi$ , the TCT analog of x-ray CT sinograms is shown in Figure 9.2a. Finally, time-series data measured by a single transducer near the equator is plotted in Figure 9.2b. Reconstructions of zero-filled partial-scan data suffer severe shading, which obscures the low-contrast occlusions. Extending partial-scan data by enforcing consistency conditions reduces low-frequency errors, reducing window width and improving visibility of low contrast inclusions.

The backprojection step applies the adjoint operator to the Radon transform and therefore annihilates all errors that lie outside the range. Therefore, enforcing consistency conditions upon complete scan data typically does not improve IQ [53]. In this case, however, consistently extending partial-scan data

**TABLE 9.1**  
**Centers, Eccentricities, and Weight for Test Phantom**

Sphere Number	Center	Radius	Weight
1	(0,0,0)	0.9	1
2	(0,0,0)	0.03125	0.1
$n=3, \dots, 6$	$0.2 (0, \cos(n\pi/2), \sin(n\pi/2))$	0.03125	0.1
$n=7, \dots, 14$	$0.4 (0, \cos(n\pi/4), \sin(n\pi/4))$	0.03125	0.1
$n=5, \dots, 26$	$0.6 (0, \cos(n\pi/6), \sin(n\pi/6))$	0.03125	0.1
$n=7, \dots, 42$	$0.8 (0, \cos(n\pi/8), \sin(n\pi/8))$	0.03125	0.1

*Note:* The spherical background has constant density,  $f=1$ , and inclusions have 10% contrast,  $f=1.1$ .

AU: Please insert Figure number.

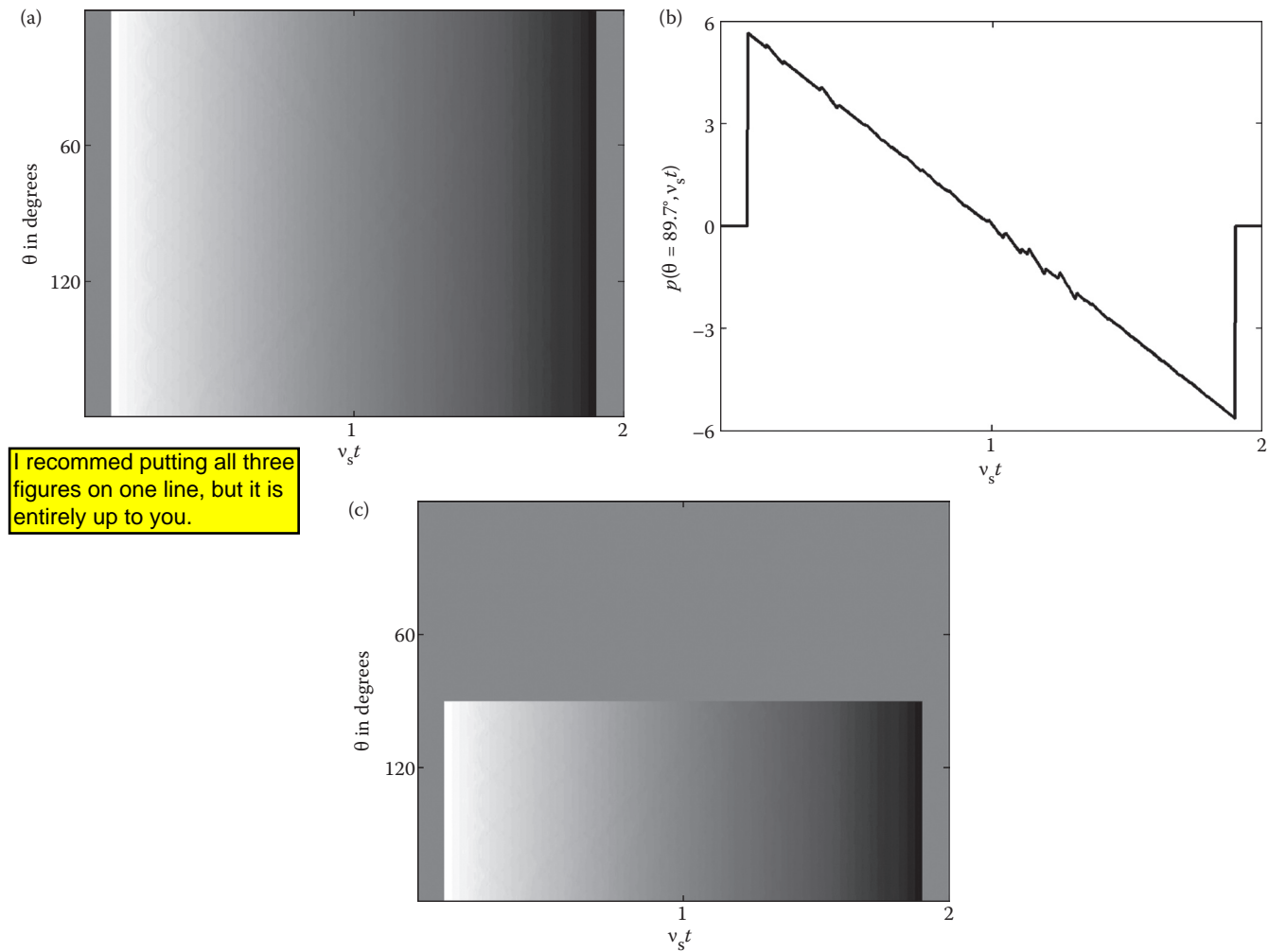
let's forget the figure label

AU: Change to 'thereby annihilating'?

OK with me

apologies - this "5" should be "15"

?? for SKP - do I not have inclusions on the perpendicular planes?!?!



I recommed putting all three figures on one line, but it is entirely up to you.

FIGURE 9.2 TCT pressures in the  $x_1-x_3$  plane where  $\phi=0$ .

adds signal to the data input into the reconstruction algorithm, increasing signal in the reconstructed image. Measurement errors may also propagate into estimated data, but the moment conditions are necessary and sufficient conditions upon the TCT transform, so enforcing them provides the most physically consistent method for estimating unmeasured data. The implementation presented below robustly estimates low frequencies in unmeasured data. It is, therefore, extremely robust to high-frequency noise, but may propagate low-frequency measurement errors into estimates of unmeasured data.

### 9.2 THEORY: CONSISTENCY CONDITIONS ON MEASURED PRESSURES

We work with consistency conditions upon idealized TCT data that are direct analogs to the moment conditions upon the standard Radon transform and are derived for  $R_{TCT}$  in Ref. [12]. We use them to derive similar moment conditions upon measured pressures,  $p(\mathbf{x}, t)$ , in Theorem 9.2.1. To provide theoretical background for this work, several recent results are restated for this particular problem. A strong sufficiency result stated in terms of monomial moment conditions is copied from Ref. [11] in Theorem 9.2.2. In Corollary 9.2.1, we

restate these consistency conditions in a form that is similar to additional conditions that completely characterize the range, as recited in Theorem 9.2.3. The section closes with a brief comparison of the conditions and their relative strengths.

**Theorem 9.2.1** *TCT pressures generated according to Equation 9.1 can be expanded as a Legendre series for each transducer location  $\mathbf{x}$  with only even terms*

$$p(\mathbf{x}, t) = \sum_{k=0}^{\infty} c_k(\mathbf{x}) P_{2k}(t) \tag{9.5}$$

where the coefficients,  $c_k(\mathbf{x})$ , are inhomogeneous polynomials of degree  $2(k-1)$  in terms of the elements of  $\mathbf{x}$ . Restricting  $\mathbf{x}$  to the surface of a sphere,  $\|\mathbf{x}\| = \rho$ , implies  $\deg c_k \leq (k-1)$ .

**Proof** For simplicity, rescale so that  $S = \{\mathbf{x} \mid \|\mathbf{x}\| = 1/2\}$  and  $\text{supp } A_e \subset B_{1/2}$ . Furthermore, take the even extension of  $R_{TCT}$  with respect to  $t$ , which therefore suggests an even extension of  $p$  with respect to  $t$ ,  $p(\mathbf{x}, -t) = p(\mathbf{x}, t)$  with support only for  $t \in [-1, 1]$ . For each transducer location  $\mathbf{x}$ ,  $c_k(\mathbf{x})$  are the standard Legendre coefficients

AU: Please clarify.  
? what am I to clarify?

I suggest not italicizing the circled "x"s for consistency.

$$\begin{aligned}
 c_k(\mathbf{x}) &= \left(\frac{4k+1}{2}\right) \int_{-1}^1 p(\mathbf{x},t) P_{2k}(t) dt \\
 &= (4k+1) \int_0^1 \frac{\partial}{\partial t} \left(\frac{1}{t} R_{\text{TCT}} A_e(\mathbf{x},t)\right) P_{2k}(t) dt \\
 &= (4k+1) \left[ \frac{R_{\text{TCT}} A_e(\mathbf{x},t)}{t} P_{2k}(t) \right]_0^1 \\
 &\quad - \int_0^1 \frac{R_{\text{TCT}} A_e(\mathbf{x},t)}{t} P'_{2k}(t) dt \\
 &= -(4k+1) \int_{\mathbf{y} \in \mathbf{R}^3} A_e(\mathbf{y}) \frac{P'_{2k}(|\mathbf{x}-\mathbf{y}|)}{|\mathbf{x}-\mathbf{y}|} d\mathbf{y}
 \end{aligned} \tag{9.6}$$

I'd nudge this to the right

align at "="  $= Q_{2(k-1)}(\mathbf{x})$  a polynomial of degree  $2(k-1)$  in elements of  $\mathbf{x} \in \mathbf{R}^3$  (9.7)

AU: Please clarify.

what am I to clarify?

$c_k(\mathbf{x}) = Q_{(k-1)}(\mathbf{x})$  a polynomial of degree  $(k-1)$  when  $\|\mathbf{x}\| \equiv \rho$ . (9.8)

~~end proof~~ if possible please replace "end proof" with a square

Note that Equation 9.7 holds because  $P_{2k}(t)$  is an even polynomial of degree  $2k$  in  $t$  so  $(P'_{2k}(t)/t)$  is also an even polynomial of degree  $2(k-1)$  in  $t$ . As noted in Ref. [11], if monomial moments of data measured on the sphere extend from the sphere to its interior as described below, then the measurements represent thermoacoustic pressures. The theorem is restated below for measured pressures in three dimensions,

**Theorem 9.2.2** Let  $p(\mathbf{x}, t) \in C^\infty(S \times [0,1])$  be measured data on the sphere of radius  $1/2$ . Then  $p$  represents measured pressures generated by some source function  $A_e(\mathbf{x})$  iff the monomial moments

$$M_k(\mathbf{x}) = \frac{1}{2-2k} \int_0^1 p(\mathbf{x},t) t^{2k-2} dt, \tag{9.9}$$

extend from the sphere to its interior as polynomials bounded by  $|M_k^{\text{ext}}| < C^k$  for some constant  $C$  and also satisfy the recurrence relation

$$\Delta M_k(\mathbf{x}) = 2k(2k+1). \tag{9.10}$$

Another way to state the conditions used to derive 1 is given below for comparison to a larger set of conditions.

**Corollary 9.2.1** TCT pressures generated according to Equation 9.1 satisfy

$$0 = \int_{\mathbf{x} \in S} \Phi_m^k(\mathbf{x}) \int_{t=-1}^1 P_{2l}(t) p(\mathbf{x},t) dt d\mathbf{x}, \tag{9.11}$$

where  $\Phi_m^k$  is a spherical harmonic of degree  $k$  and  $l=0,1,2,\dots,(k-1)$ .

Different conditions that are both necessary and sufficient for measured data to represent thermoacoustic pressures are derived in Ref. [52].

**Theorem 9.2.3**  $p(\mathbf{x}, t) \in C^\infty(S \times \mathbf{R}^+)$  is in the range of the TCT transform for  $\mathbf{x}$ , iff

$$0 = \int_{\mathbf{x} \in S} \Phi_m^k(\mathbf{x}) \int_{t=0}^1 \cos(\omega_l t) p(\mathbf{x},t) dt d\mathbf{x}, \tag{9.12}$$

where  $\Phi_m^k$  is a spherical harmonic of degree  $k$ ,  $\omega_l > 0$  is a root of the Bessel function  $J_{k+1/2}(\omega/2)$ , and  $S$  is the sphere of radius  $1/2$ .

In Corollary 9.2.1, a particular spherical harmonic  $\Phi_m^k$  of degree  $k$  is orthogonal to exactly  $(k+1)$  moments of the measured pressure,  $\int_{t=-1}^1 P_{2l}(t) p(\mathbf{x},t) dt$  for  $l=0,1,2,\dots,k$ . In contrast, Theorem 9.2.3 implies that  $\Phi_m^k$  is orthogonal to infinitely many weighted integrals of  $p$ ,  $\int_{t=-1}^1 \cos(\omega_l t) p(\mathbf{x},t) dt$  for  $l=0,1,2,\dots,\infty$ . Fortunately, the necessary and sufficient monomial moment conditions in Theorem 9.2.2 are equivalent to those enforced in Theorem 9.2.1.

### 9.3 APPLICATION: CONSISTENCY CONDITIONS ON MEASURED PRESSURES

The simpler moment conditions in Theorem 9.2.1 are enforced to consistently extend partial-scan data, adding low-frequency signal where there would otherwise be zero-valued data. Zero-filling partial-scan data for unmeasured transducer locations truncates coefficients,  $c_k(\mathbf{x})$ , converting them from low-order polynomials to very high-order functions, as shown in Figure 9.3. The DC coefficient is always zero,  $c_0(\mathbf{x}) \equiv 0$ , and  $c_1(\mathbf{x})$  is a nonzero constant

$$c_1(\mathbf{x}) = -5 \int_{\mathbf{y} \in \mathbf{R}^3} A_e(\mathbf{y}) 3d\mathbf{y} \quad \forall \mathbf{x} \tag{9.13}$$

$C_1$  is a polynomial of degree zero, whereas for zero-filled partial-scan data  $c_1^{\text{PS}}(\mathbf{x})$  has a sharp discontinuity with respect to  $\mathbf{x}$  at the equator, and is therefore no longer a constant. Although the expansion of  $c_1^{\text{PS}}(\mathbf{x}(\phi, \theta))$  is independent of  $\phi$ , it is a complicated function of  $\theta$

$$c_1^{\text{PS}}(\mathbf{x}) = -15 \|A_e\|_{L^1} \chi_{\mathbf{x} \in S_-^2}(\mathbf{x}) = \sum_{\forall \alpha} c_1^\alpha \cos \theta, \tag{9.14}$$

where

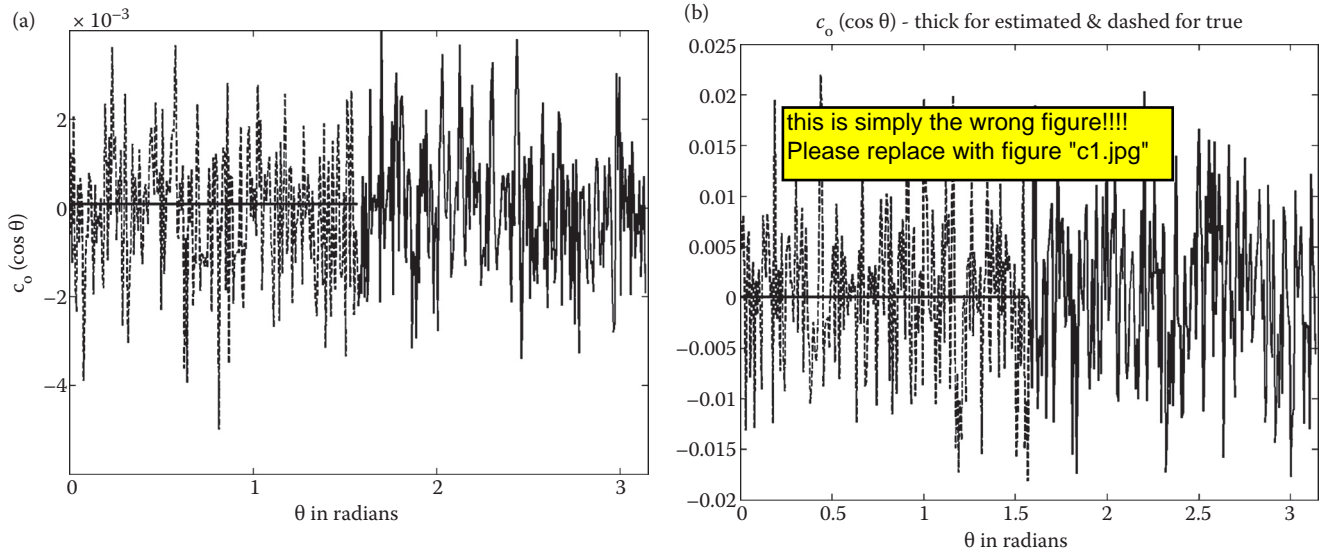
$$\mathbf{x} = \frac{1}{2} \begin{pmatrix} \sin \theta \cos \phi \\ \sin \theta \sin \phi \\ \cos \theta \end{pmatrix}$$

and

$$\chi_{\mathbf{x} \in S_-^2}(\mathbf{x}) = \begin{cases} 1 & \text{for } \mathbf{x} \in S_-^2 \\ 0 & \text{otherwise} \end{cases}$$

is the indicator function supported on the lower hemisphere,  $S_-^2$ . With this scaling,  $t \in [0,1]$  and for each transducer location, the data  $p(\mathbf{x},t)$  are sampled with very high frequency in  $t$ . From these measurements, we first estimate  $c_k(\mathbf{x})$  for all measured transducer locations  $\theta_i \in [\pi/2, \pi]$  and  $\phi_j \in [\pi/2, \pi]$  from Equation 9.6. (Note that if the measurement sphere were of a different radius, the coefficients in Equation 9.13 and Equation 9.14 would change but the principle would still

AU: Following terms have been displayed as they are too large for text equations.



AU: Please clarify. Is it 'thick-dashed'?

**FIGURE 9.3** Coefficients of zero-filled partial-scan data are truncated polynomials. Noisy partial-scan measurements at  $\phi=0$  with  $\sigma_{\text{abs}}=0.25$  in thin-solid; complete data in thin-dashed; estimated in thick.

apply.) The next step is to exploit the fact that  $c_k$  is a (real-valued) polynomial of degree  $(k-1)$  in the coordinates of  $\mathbf{x} \in S$ , decomposing  $c_k$  into spherical harmonics

$$c_k(\mathbf{x}(\theta, \phi)) = \sum_{l=0}^{(k-1)} \sum_{m=-l}^l d_k^{l,m} P_l^{|m|}(\cos \theta) e^{im\phi}. \quad (9.15)$$

In an ideal situation, noise-free measurements are made for all points on  $S_-$  and from *all* of these measurements  $\{d_k^{l,m}\}_{k,l,m}$  is accurately estimated. Knowledge of  $\{d_k^{l,m}\}_{k,l,m}$  allows us to evaluate  $c_k$  on  $S_+$ , and plugging into Equation 9.5 we evaluate  $p(\mathbf{x}, t)$  for  $\mathbf{x} \in S_+$ . For computational simplicity, results are presented for phantoms symmetric with respect to  $\phi$ :

$$\begin{aligned} A_c(\mathbf{x}(r; \theta, \phi)) &= A_c(\mathbf{x}(r; \theta, -\phi)) = A_c(\mathbf{x}(r; \theta, \pi + \phi)) \\ &= A_c(\mathbf{x}(r; \theta, \pi - \phi)), \end{aligned} \quad (9.16)$$

which implies symmetries on pressures measured on the sphere  $r=|\mathbf{x}|=1$

$$\begin{aligned} p(\mathbf{x}(\theta, \phi), t) &= p(\mathbf{x}(\theta, -\phi), t) = p(\mathbf{x}(\theta, \pi + \phi), t) \\ &= p(\mathbf{x}(\theta, \pi - \phi), t), \end{aligned} \quad (9.17)$$

using these facts along with the fact that for our experiments  $p(\mathbf{x}, t) \in \mathbf{R}$  the expansions for coefficients  $c_k$  can be simplified compared to Equation 9.15

$$c_k(\mathbf{x}(\theta, \phi)) = \sum_{l=0}^{(k-1)} \left[ \tilde{d}_k^{l,0} P_l(\cos \theta) + 2 \sum_{m=1}^{fl(l/2)} \tilde{d}_k^{l,2m} P_l^{2m}(\cos \theta) \cos 2m\phi \right], \quad (9.18)$$

where  $fl$  is the *floor* function.  $P_l^{2m}$  are polynomials, so  $c_k$  is a polynomial with respect to  $\cos \theta = x_3$  for fixed  $\phi$

$$c_k(\mathbf{x}(\theta, \phi)) = \sum_{l=0}^{(k-1)} \hat{d}_k^l(\phi) P_l(\cos \theta). \quad (9.19)$$

For the measured partial-scan data  $\mathbf{x} \in S_-$  so  $x_3 = \cos \theta \in [-1, 0]$  because  $\theta \in [\pi/2, \pi]$ . Rescaling makes  $c_k$  into a new polynomial over the interval  $[-1, 1]$ . Let

$$\tilde{x} = 2x_3 + 1 \in [-1, 1], \quad (9.20)$$

$$c_k(\mathbf{x}) = c_k(\tilde{x}, \phi) = \sum_{l=0}^k \hat{d}_k^l(\phi) P_l(\tilde{x}) \quad \text{where} \quad \hat{d}_k^l \neq d_k^l. \quad (9.21)$$

Numerically integrating  $c_k(\tilde{x}, \phi)$  against  $(P_l(\tilde{x}) / (2l(2l+1)))$  for  $l=0, 1, 2, \dots, (k-1)$  computes  $\hat{d}_k^l(\phi)$ .

$$\hat{d}_k^l(\phi) = \left( \frac{2l+1}{2} \right) \int_{-1}^1 c_k(\tilde{x}, \phi) P_l(\tilde{x}) d\tilde{x}. \quad (9.22)$$

## 9.4 NUMERICAL METHODS

Many parts of human anatomy are nearly piecewise constant with respect to the x-ray linear attenuation coefficient. Reconstructions of backprojection type tend to suffer streak artifacts off of edges, so phantoms with jump discontinuities are difficult to reconstruct accurately. Therefore, piecewise constant phantoms are commonly used to test standard x-ray CT reconstruction algorithms, and we also consider a piecewise constant phantom. Although  $R_{\text{TCI}}(\mathbf{x}, t)$  is continuous with respect to  $t$  for most physiologically relevant piecewise constant phantom functions, measured pressures are often discontinuous with respect to  $t$  as shown in Figure 9.2b. Polynomial expansions of measured pressures may therefore converge slowly and high-order polynomial expansions are required to accurately model measured pressures according to Equation 9.5. We sample at finitely many times,  $t_j$ , and can therefore estimate a limited number of coefficients  $c_k(\mathbf{x})$  for each transducer location,  $\mathbf{x}$ . Furthermore, we sample only finitely many  $\mathbf{x} \in S_-$  and measured data always contains noise. Therefore, we recover at best a band-limited representation,  $\{d_k^{l,m}\}_{k \leq K}$ .

AU: Please clarify.

what am I to clarify?

In the results presented below, images are reconstructed by implementing the FBP Formula 9.3 as described in Ref. [15]. The phantom as described in Table 9.1, is a sum of indicator functions on spheres so data are computed analytically by evaluating Equation 9.2. A spherical inclusion of radius  $a$  centered a distance  $L$  from transducer location  $\mathbf{x}$  generates the pressure

$$p(\mathbf{x}, t) = \left( \frac{\partial}{\partial t} \right) \frac{\pi a}{L} [(L-t)^2 - a^2] \chi_{|L-t| < a}(t) = 2\pi \left[ 1 - \frac{t}{L} \right] \chi_{|L-t| < a}(t).$$

This formula was evaluated numerically, assuming transducer locations at 400 Gaussian quadrature nodes  $x_{3,i} = \cos \theta_i \in [-1, 1]$  and 800 equally spaced angles  $\phi_j = 2\pi(j/800)$ . Partial-scan data has only transducers placed at 200 of 400 Gaussian quadrature nodes  $\cos \theta_i \in [-1, 0]$ . Each transducer samples with respect to the radial variable so that  $\Delta t = 1/512$ . Centered finite differences, Gaussian quadrature with respect to  $\cos \theta$ , and the trapezoid rule with respect to  $\phi$  were used to evaluate the inversion Formula 9.3. Noisy data reconstructions shown in this section correspond to additive white noise with  $\sigma_{\text{abs}} = 0.25$  where

$$p_{\text{noisy}}(\mathbf{x}(\theta_i, \phi_j), t_k) = p_{\text{true}}(\mathbf{x}(\theta_i, \phi_j), t_k) + \sigma_{\text{abs}} X, \quad (9.23)$$

where  $X \sim N(0,1)$  is a Gaussian random variable with mean zero and standard deviation 1 realized for each measurement point  $(\theta_i, \phi_j, t_k)$  using MATLAB®'s **randn** number generator, "randn".

### 9.4.1 COMPUTING MOMENTS, $c_k(\mathbf{x})$

Because  $p(\mathbf{x}, t)$  is discontinuous with respect to  $t$ , Equation 9.6 was evaluated using the Trapezoid rule where  $v_s \Delta t = 1/512$ . Higher order methods are even more unstable with respect to jumps in the integrand, however. Note that, in practice, sampling rates on the order of  $2E^{-9}s = 2 \text{ ns}$  are possible, yielding  $v_s \Delta t = 1.5 \text{ mm}/\mu\text{s} \times 2E^{-9}s = 3 \mu\text{m}$ . Ideal and noisy time series are plotted in Figure 9.4d and 9e. Estimating Legendre coefficients according to Equation 9.6 results in an additive error according to

$$c_{k,\text{noisy}}(\mathbf{x}) = c_k(\mathbf{x}) + \sigma_{\text{abs}} \frac{(4k+1)}{2} \int_{-1}^1 X(t) P_{2k}(t) dt. \quad (9.24)$$

Clearly, the expected value of the 0th order coefficient is the true value,  $E(c_{0,\text{noisy}}) = c_0$  and estimates of low order coefficients are robust to additive white noise. The statistical properties of error in numerical estimates can be analyzed

$$c_{k,\text{noisy}}^{\text{num}}(\mathbf{x}) = c_k^{\text{num}}(\mathbf{x}) + \sigma_{\text{abs}} \frac{(4k+1)}{N_t} \sum_{k=1}^{N_t} X(t_k) P_{2k}(t_k) = c_k^{\text{num}}(\mathbf{x}) + \sigma_{\text{abs}} (4k+1) \tilde{X}, \quad (9.25)$$

if possible please label the axes as shown, similar to labels in Figure 9.2a and 9.2c

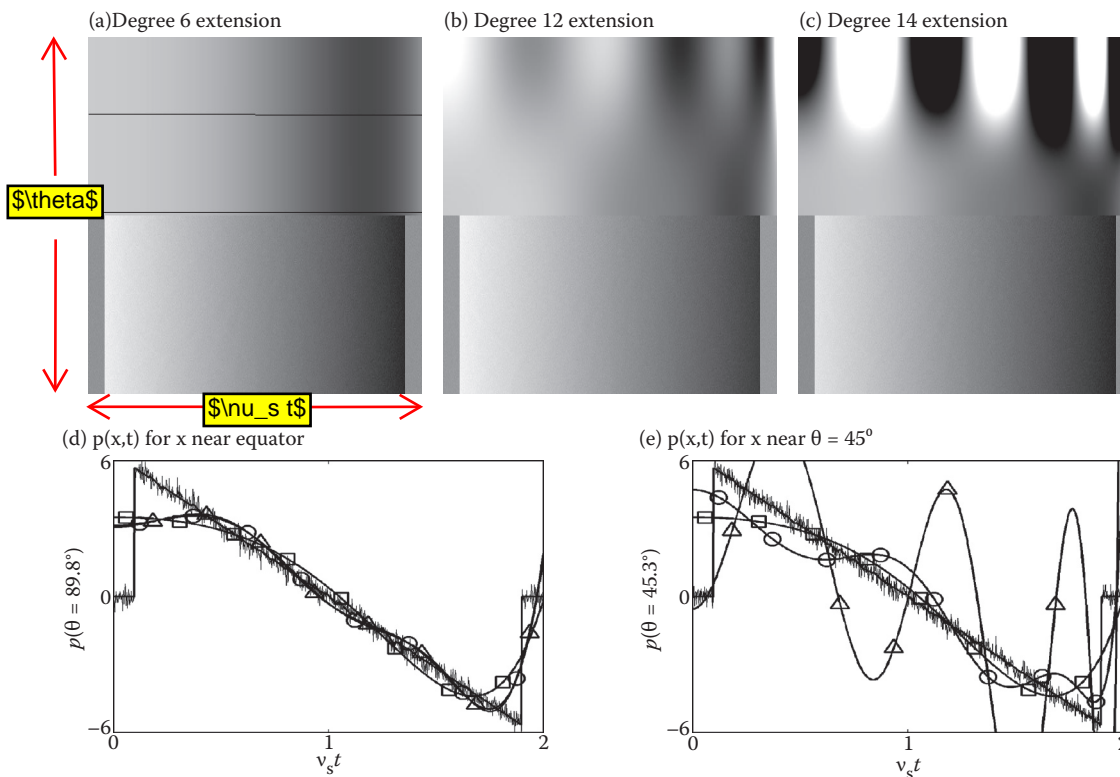


**FIGURE 9.4** Noisy pressures  $w/\sigma_{\text{abs}}=0.25$  measured below the equator and extended above the equator. (a) Horizontal lines denote extended data plotted in (d) and (e), where thick and thin solid lines denote noise-free and noisy measurements; Symbols  $\square$ ,  $\circ$ , and  $\triangle$

AU: Please verify that this amendment is permissible.

where  $\tilde{X} \sim N(0, \sigma^2)$  and  $\sigma^2 = 1/N_t \sum_{k=1}^{N_t} P_{2k}^2(t_k) \sim \|P_{2k}\|^2$ . Although the variances of the error term increases with data extension order,  $k$ , the expected value remains zero.

**9.4.2 COMPUTING COEFFICIENTS  $d_k^l(\phi)$**

Measured data are sampled on standard Gaussian quadrature nodes  $[-1,1]$ , but only samples within the subinterval  $x_3 \in [-1,0]$  are measured. To evaluate Equation 9.22, we first linearly interpolated measurements for  $x_3 \in [-1,0]$  onto Gaussian quadrature nodes for  $\tilde{x} \in [-1,1]$ . Results presented here were computed by interpolating a subset of 200 Gaussian quadrature nodes  $x_{3,i} = \cos\theta_i \in [-1,0]$  onto a complete set of 200 Gaussian quadrature nodes  $\tilde{x}_j \in [-1,1]$ . This low-order interpolation contributes significantly to errors in the data extensions shown in Figure 9.4. Equation 9.22 was then evaluated using Gaussian quadrature, which is exact for low-degree polynomials and would therefore be mathematically exact for a true estimate if  $c_k(\tilde{x}, \phi)$  is a polynomial in  $\tilde{x}$ .

**9.4.3 ESTIMATING UNMEASURED PRESSURES  $p(x_3, \phi, t)$ : STABILITY AND COMPUTATIONAL COST**

Plugging the coefficients  $d_k^l$  back into Equations 9.21 and 9.5 allows us to evaluate at the unmeasured transducer locations  $\mathbf{x} \in S^+$  where  $\tilde{x} \in [1,3]$

$$p(\tilde{x}, \phi, t) = \sum_{k=0}^{XDeg} c_k(\tilde{x}, \phi) P_{2k}(t) = \sum_{k=0}^{XDeg} P_{2k}(t) \left( \sum_{l=0}^k d_k^l(\phi) P_l(\tilde{x}) \right), \quad (9.26)$$

where  $d_k^l$  are computed from Equation 9.22. Extensions of half-scan data are shown in Figure 9.4 for extension degrees,  $XDeg=6, 12,$  and  $14$ .

**9.4.3.1 Stability**

This is where instability of analytic continuation reveals itself. Errors in estimates of  $d_k^l$  are amplified because Legendre polynomials tend to blow up outside of the fit interval  $[-1,1]$  and we evaluate for  $\tilde{x} \in [1,3]$ . See Figure 9.5 for plots

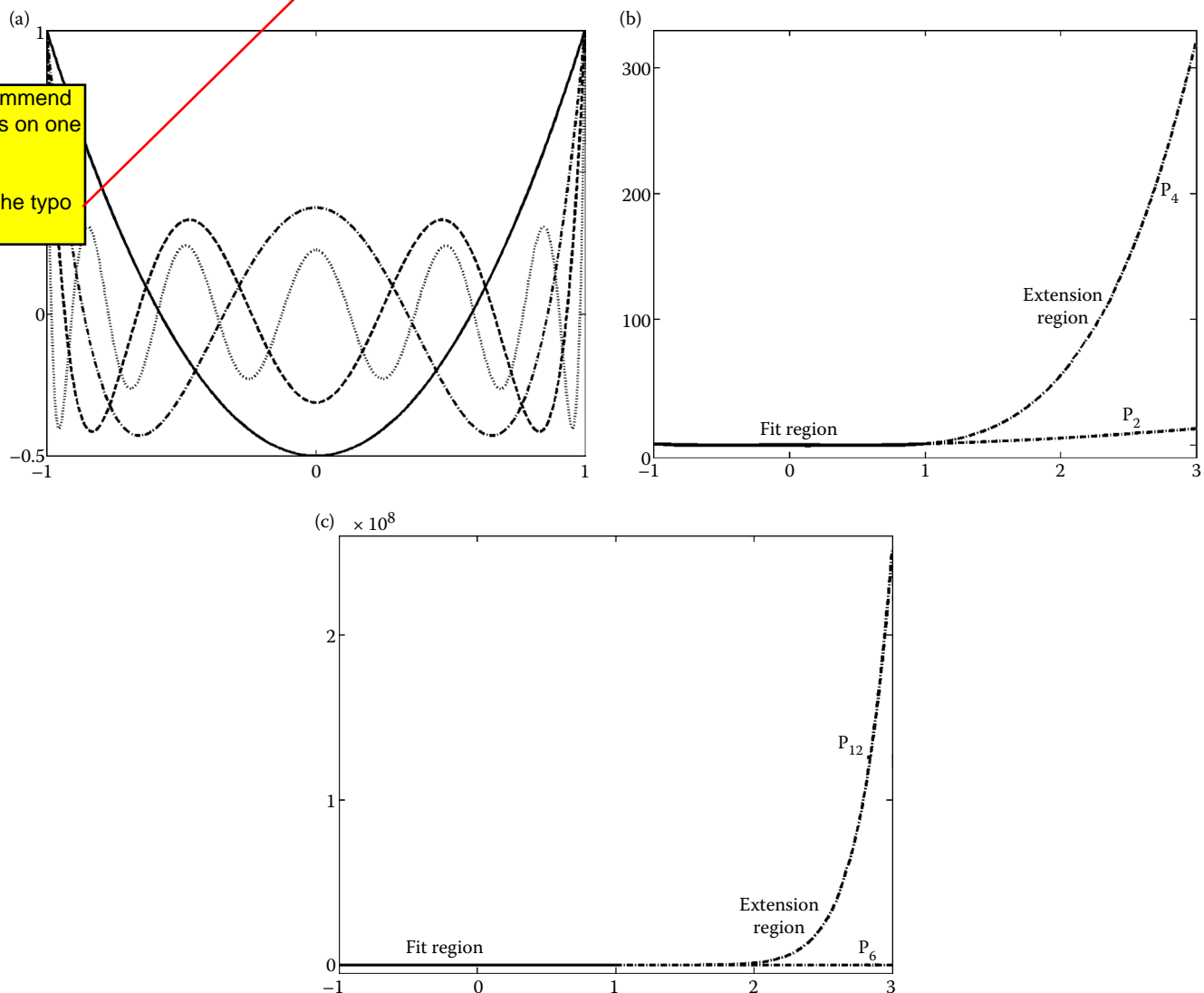


**FIGURE 9.5** Legendre polynomials are orthogonal and bounded over the interval  $[-1,1]$ , but blow up in the extension region  $[1,3]$ .

once again, I recommend putting all 3 figures on one line if you can  
ALSO, please fix the typo indicated above.

demonstrating the blowup of Legendre polynomials evaluated beyond the interval  $[-1,1]$ . Corresponding blowup can be seen in extensions of noisy Defrise data in Figure 9.4. This instability limits the order,  $XDeg$ , of the fit we seek. Results presented below are for  $XDeg=0, 6, 12, 14$ .

**9.4.3.2 Computational Cost**

Evaluating Equation 9.26 for all unmeasured transducer locations is relatively cheap compared to the cost of image reconstruction. Order of magnitude estimates for each step are listed in Table 9.2. Here  $N_\theta=400, N_\phi=800, N_t=1,024$ , and  $XDeg \leq 14$ . The order of magnitude flop (floating point operations) count is  $O(N_t N_\theta N_\phi XDeg)$ , which is far less costly

than the  $O(N^3 N_\theta N_\phi)$  cost of backprojecting onto an  $N^3$  reconstruction volume.

**9.5 NUMERICAL RESULTS**

Reconstructions of the  $\phi=0$  plane from all combinations of noise-free and noisy vs. complete and zero-filled, partial-scan data are shown in Figure 9.6. Noise is additive white noise with  $\sigma_{abs}=0.25$  and  $\max p(\mathbf{x},t) \sim 2\pi \times 0.9 = 5.7$ . Zero-filled partial-scan reconstructions, i.e., with  $XDeg=0$ , show affine shading in the vertical direction. Inclusions that are clearly detectable in the full scan reconstructions are barely discernable in the noise-free half-scan reconstruction and are lost entirely when noisy half-scan data is zero-filled. Reconstructions of noisy partial-scan data extended to varying degrees are displayed in Figure 9.7. Even the lowest order extension of degree 6 corrects the low-frequency shading sufficiently so that all inclusions are visible. The degree-14 extension becomes unstable in the presence of noise, but extensions of degree 12 and lower are stable and drastically improve IQ, making most low-contrast inclusions visible. Profiles along the  $x_3$ -axis plotted in Figure 9.7d demonstrate that low-frequency extension of partial-scan data reduces low-frequency shading without enhancing noise in reconstructions below the equator. Reconstructions above the equator quickly become unstable, as indicated by the profile for  $XDeg=14$ .

**TABLE 9.2**  
**Order of Magnitude Flop Counts for Various Steps in Data Extension**

Evaluate	Description	No. Flops
Moments in Equation 9.21	Quadrature wrt $t$	$N_t N_\theta N_\phi XDeg$
Evaluate on Gauss quad nodes	Interpolate wrt $\bar{x}$	$N_\theta N_\phi XDeg$
$d_k^l(\phi)$ in Equation 9.22	Quadrature wrt $\bar{x}$	$N_\theta N_\phi XDeg^2$
Right-most sums in Equation 9.26	Summations	$N_\theta N_\phi XDeg^2$
Equation 9.26	Summations	$N_t N_\theta N_\phi XDeg$

AU: Numbers refer to equations?  
**YES**

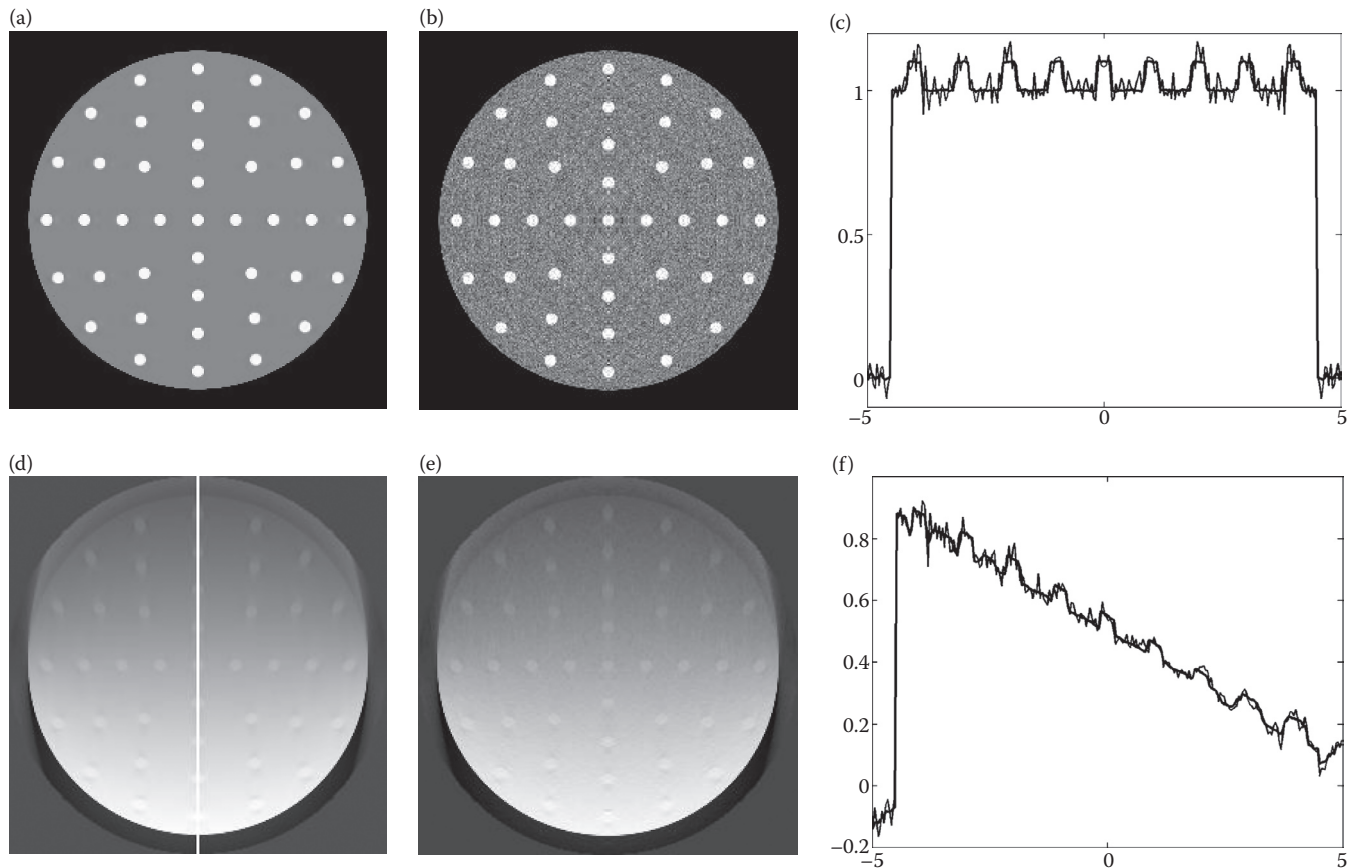
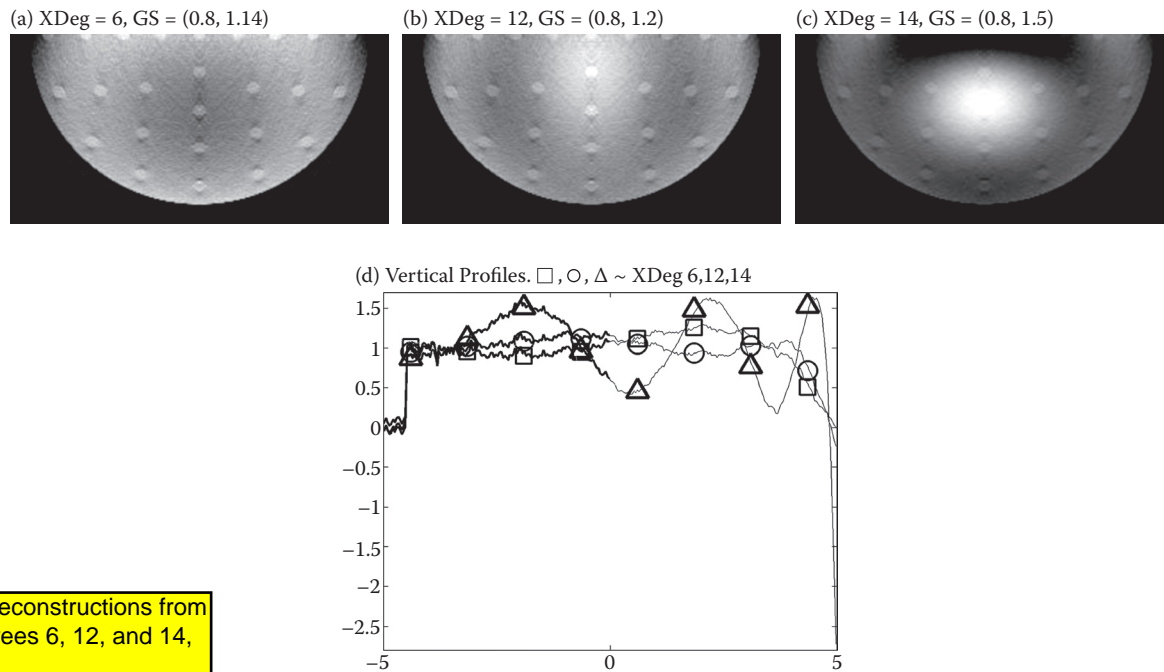


**FIGURE 9.6** FBP reconstructions. Bottom-most inclusions are not well-defined by the half-scan reconstructions in (d) and (e). Vertical profile taken along white line in (d).

AU: Please provide details for part labels a, b, and c.

Reconstructions from full scan data without and with noise in (a) and (b), respectively. Reconstructions of zero-filled half scan data without and with noise in (d) and (e). V



(a), (b), and (c) show reconstructions from data extended to degrees 6, 12, and 14, respectively.

AU: Please provide details for part labels a, b, and c.

**FIGURE 9.7** Reconstructions of ROI below equator from  $\sigma_{\text{abs}}=0.25$  half-scan data extended to orders 6, 12, and 14. (d) Vertical profiles. Thick in ROI, thin above equator where  $x_3 > 0$ .

This is not surprising because data is estimated most stably for transducer locations near the equator, as depicted in Figure 9.4. As one moves further from the measurement surface  $S_-$ , the more difficult it becomes to estimate unmeasured pressures. Furthermore, the FBP inversion Formula 9.3 preferentially weights measurements taken close to the reconstruction point  $\mathbf{x}$ . On average, for reconstruction points below the equator, measured data is weighted more heavily than estimated data. Furthermore, stably estimated data corresponding to transducer locations near the equator is weighted more heavily than data estimated for transducer locations near the north pole.

## 9.6 CONCLUSIONS

We have shown that partial-scan reconstructions of TCT data agree with theoretical predictions from integral geometry. Low-frequency shading degrades IQ when partial-scan data is naïvely reconstructed by zero-filling missing data, as demonstrated in Figure 9.6d and e. Strong, but low-frequency shading across zero-filled partial-scan reconstructions can obscure low-contrast inclusions. Low-frequency extension of partial-scan data by enforcing consistency conditions upon TCT data can remove low-frequency shading and therefore improve visibility of small, low-contrast inclusions.

Data extension by enforcing moment conditions up to degree 12 drastically reduced low-frequency shading and is robust to additive white noise in measured data. We demonstrated this by using phantoms with sufficient symmetry to greatly simplify data fitting. Clinical implementation of this data extension method requires generalizing the data

fits to asymmetric objects and fitting data for all transducer locations simultaneously, i.e., over all  $(\theta_i, \phi_j)$ .

This work shows that extensions up to degree 12 are feasible and can improve visibility of low-contrast lesions over simple zero filling with minimal computational cost. This method of data extension could perhaps be used to quickly generate a good initial image for computationally costly iterative methods, thereby reducing the number of iterations required for high-quality image reconstruction.

## REFERENCES

1. Kruger, R.A., K.D. Miller, H.E. Reynolds, W.L. Kiser Jr., D.R. Reinecke, and G.A. Kruger. 2000. Contrast enhancement of breast cancer *in vivo* using thermoacoustic CT at 434 MHz. *Radiology* 216:279–83.
2. Kruger, R.A., K.K. Kopecky, A.M. Aisen, D.R. Reinecke, G.A. Kruger, and W.L. Kiser Jr. 1999. Thermoacoustic CT with radio waves: A medical imaging paradigm. *Radiology* 211:275–78.
3. Kruger, R.A., D.R. Reinecke, and G.A. Kruger. 1999. Thermoacoustic computed tomography. *Med. Phys.* 26(9): 1832–37.
4. Kruger, R.A., P. Liu, Y.R. Fang, and C.R. Appledorn. 1995. Photoacoustic ultrasound (PAUS) – reconstruction tomography. *Med. Phys.* 22(10):1605–609.
5. Xu, M., and L.V. Wang. 2002. Time-domain reconstruction for thermoacoustic tomography in a spherical geometry. *IEEE Trans. Med. Imaging* 21(7):814–22.
6. Norton, S.J., and T. Vo-Dinh. 2003. Photoacoustic diffraction tomography: Analysis of algorithms. *J. Opt. Soc. Am. A* 20(10):1859–66.
7. Liu, P. 1998. The  $P$ -transform and photoacoustic image reconstruction. *Phys. Med. Biol.* 43:667–74.

8. Manohar, S., A. Kharine, J.C.G. van Hespén, W. Steenbergen, and T.G. van Leeuwen. 2005. The Twente photoacoustic mammoscope: System overview and performance. *Phys. Med. Biol.* 50:2543–57.
9. Manohar, S., A. Kharine, J.C.G. van Hespén, W. Steenbergen, and T.G. van Leeuwen. 2004. Photoacoustic mammography laboratory prototype: Imaging of breast tissue phantoms. *J. Biomed. Opt.* 9(6):1172–81.
10. Esenaliev, R.E., A.A. Karabutov, and A.O. Oraevsky. 1999. Sensitivity of laser opto-acoustic imaging in detection of small deeply embedded tumors. *IEEE J. Select. Top. Quantum Electron.: Laser Biol. Med.* 5(4):981–88.
11. Agranovsky, M.L., P. Kuchment, and E.T. Quinto. 2007. Range descriptions for the spherical mean Radon transform. *J. Funct. Anal.* doi:10.1016/j.jfa.2007.03.022.
12. Patch, S.K. 2004. Thermoacoustic tomography – consistency conditions and the partial scan problem. *Phys. Med. Biol.* 49(11):2305–15.
13. Gusev, V.E., and A.A. Karabutov. 1993. *Laser optoacoustics*. New York: American Institute of Physics.
14. Finch, D.V., S.K. Patch, and Rakesh. 2004. Determining a function from its mean values of a family of spheres. *SIAM J. Math. Anal.* 35(5):1213–40.
15. Ambartsoumian, G., and S.K. Patch. 2007. Thermoacoustic tomography – numerical results. *Proc. SPIE* 6437:64371B.
16. John, F. 1955. *Plane waves and spherical means applied to partial differential equations*. New York: Interscience.
17. Palamodov, V.P. 2004. *Reconstructive integral geometry*. Monographs in Mathematics Series 98. Boston, MA: Birkhäuser.
18. Natterer, F., and F. Wübbeling. 2001. *Mathematical methods in image reconstruction*. Philadelphia, PA: Society for Industrial and Applied Mathematics.
- Finch, D., and Rakesh. The spherical mean value operator with centers on a sphere. *Inverse Problems*. (Accepted).
- Kuchment, P., and L. Kunyansky. 2007. Mathematics of thermoacoustic and photoacoustic tomography. *ArXiv* 0704.0286v1 (April). <http://arxiv.org/abs/0704.0286>.
- Fawcett, J.A. 1985. Inversion of  $N$ -dimensional spherical averages. *SIAM J. Appl. Math.* 45(2):336–41.
- Norton, S.J. 1980. Reconstruction of a two-dimensional reflecting medium over a circular domain: Exact solution. *J. Acoust. Soc. Am.* 67(4):1266–73.
- Norton, S.J., and M. Linzer. 1981. Ultrasonic reflectivity imaging in three dimensions: Exact inverse scattering solutions for plane, cylindrical, and spherical apertures. *IEEE Trans. Biomed. Eng.* 28:200–202.
- Cormack, A. 1963. Representation of a function by its line integrals, with some radiological applications. *J. Appl. Phys.* 34(9):2722–27.
- Cormack, A. 1964. Representation of a function by its line integrals, with some radiological applications II. *J. Appl. Phys.* 35(10):2908–13.
- Xu, M., and L. V. Wang. 2005. Universal back-projection algorithm for photoacoustic computed tomography. *Phys. Rev. E* 71:016706.
- Finch, D.V., M. Haltmeier, and Rakesh. Inversion of spherical means and the wave equation in even dimensions. *SIAM J. Appl. Math.* Submitted.
- Kunyansky, L.A. 2007. Explicit inversion formulae for the spherical mean Radon transform. *Inverse Problems* 23:373–83.
- Kunyansky, L.A. 2008. A series solution and a fast algorithm for the inversion of the spherical mean Radon transform. *Inverse Problems*. Accepted.
- Schuster, T., and E.T. Quinto. 2005. On a regularization scheme for linear operators in distribution spaces with an application to the spherical Radon transform. *SIAM J. Appl. Math.* 65:1369–87.
31. Schuster, T. 2007. *The method of approximate inverse: Theory and applications*. Lecture Notes in Mathematics Series 1906. Berlin: Springer.
32. Haltmeier, M., T. Schuster, and O. Scherzer. 2005. Filtered backprojection for thermoacoustic computed tomography in spherical geometry. *Math. Methods Appl. Sci.* 28(16):1919–37.
33. Andreev, V.G., A.A. Karabutov, and A.A. Oraevsky. 2003. Detection of ultrawide-band ultrasound pulses in optoacoustic tomography. *IEEE Trans. Ultrason. Ferroelectr. Freq. Control* 50(10):1383–90.
34. Haltmeier, M., O. Scherzer, P. Burgholzer, and G. Paltauf. 2004. Thermoacoustic computed tomography with large planar receivers. *Inverse Problems* 20:1663–73.
35. Kostli, K.P., and P.C. Beard. 2003. Two-dimensional photoacoustic imaging by use of Fourier-transform image reconstruction and a detector with an anisotropic response. *Appl. Opt.* 42(10):1899–908.
36. Hamilton, J.D., and M. O'Donnell. 1998. High frequency ultrasound imaging with optical arrays. *IEEE Trans. Ultrason. Ferroelectr. Freq. Control* 45(1):216–35.
37. Carp, S.A., A. Guerra, S.Q. Duque, and V. Venugopalan. 2004. Optoacoustic imaging using interferometric measurement of surface displacement. *Appl. Phys. Lett.* 85(23):5772–74.
38. Beard, P.C. 2005. Two-dimensional ultrasound receive array using an angle-tuned Fabry-Perot polymer film sensor for transducer field characterization and transmission ultrasound imaging. *IEEE Trans. Ultrason. Ferroelectr. Freq. Control* 52(6):1003–12.
39. Ashkenazi, S., C.-Y. Chao, L.J. Guo, and M. O'Donnell. 2004. Ultrasound detection using polymer microring optical resonator. *Appl. Phys. Lett.* 85(22):5418–20.
40. Paltauf, G., H. Schmidt-Kloiber, K.P. Kostli, et al. 1999. Optical method for two-dimensional ultrasonic detection. *Appl. Phys. Lett.* 75(8):1048–50.
41. Paltauf, G., H. Schmidt-Kloiber, and M. Frenz. 1998. Photoacoustic waves excited in liquids by fiber-transmitted laser pulses. *J. Acoust. Soc. Am.* 104(2):890–97.
42. Paltauf, G., and H. Schmidt-Kloiber. 1997. Measurement of laser-induced acoustic waves with a calibrated optical transducer. *J. Appl. Phys.* 82(4):1525–31.
43. Paltauf, G., and H. Schmidt-Kloiber. 2000. Pulsed optoacoustic characterization of layered media. *J. Appl. Phys.* 88(3):1624–31.
44. Niederhauser, J.J., M. Jaeger, and M. Frenz. 2004. Real-time three-dimensional optoacoustic imaging using an acoustic lens system. *Appl. Phys. Lett.* 85(5):846–48.
45. Niederhauser, J.J., D. Frauchiger, H.P. Weber, et al. 2002. Real-time optoacoustic imaging using a Schlieren transducer. *Appl. Phys. Lett.* 81(4):571–73.
46. Zhang, E., and P. Beard. 2006. Broadband ultrasound field mapping system using a wavelength tuned, optically scanned focused laser beam to address a Fabry Perot polymer film sensor. *IEEE Trans. Ultrason. Ferroelectr. Freq. Control* 53(7):1330–38.
47. Jaeger, M., J.J. Niederhauser, M. Hejazi, and M. Frenz. 2005. Diffraction-free acoustic detection for optoacoustic depth profiling of tissue using an optically transparent polyvinylidene fluoride pressure transducer operated in backward and forward mode. *J. Biomed. Opt.* 10(2):024035.
48. Agranovsky, M.L., and E.T. Quinto. 1996. Injectivity sets for the Radon transform over circles and complete systems of radial functions. *J. Funct. Anal.* 139:383–414.

[Finch07] Finch D, Rakesh, "The spherical mean value operator with centers on a sphere," *Inverse Problems*, 23(6), S37-51, (2007).

do not have reference for Kuchment & Kunyansky at my fingertips

D. Finch, M. Haltmeier, Rakesh, "Inversion of spherical means and the wave equation in even dimensions," *SIAM J Appl Math* Vol 68 Issue 2, pages 392-412 (2007).

Kunyansky, L.A. 2008. A series solution and a fast algorithm for the inversion of the spherical mean Radon transform. *Inverse Problems*, 23(6), 2007.

AU: Please cite all authors.

AU: Please cite all authors.

49. Ambartsoumian, G., and P. Kuchment. 2005. On the injectivity of the circular Radon transform. *Inverse Problems* 21:473–85.
50. Agranovsky, M.L., and E.T. Quinto. 2001. Geometry of stationary sets for the wave equation in  $R^n$ : The case of finitely supported initial data. *Duke Math. J.* 107(1):57–84.
51. Ambartsoumian, G., and P. Kuchment. 2006. A range description for the planar circular Radon transform. *SIAM J. Math. Anal.* 38(2):681–92.
52. Finch, D.V., and Rakesh. 2006. The range of the spherical mean value operator for functions supported in a ball. *Inverse Problems* 22:923–38.
53. Patch, S.K. 2000. Moment conditions indirectly improve image quality. *Contemp. Math.* 278:193–205.
54. Palamodov, V.P. 2000. Reconstruction from limited data of arc means. *J. Fourier Anal. Appl.* 6(1):25–42.
55. Davison, M.E. 1983. The ill-conditioned nature of the limited angle tomography problem. *SIAM J. Appl. Math.* 43(2):428–48.
56. Davison, M.E., and F.A. Grunbaum. 1981. Tomographic reconstruction with arbitrary directions. *Commun. Pure Appl. Math.* 34(1):77–119.
57. Xu, Y., L. Wang, G. Ambartsoumian, and P. Kuchment. 2004. Reconstructions in limited view thermoacoustic tomography. *Med. Phys.* 31(4):724–33.
58. Louis, A.K., and E.T. Quinto. 2000. Local tomographic methods in SONAR. In *Surveys on solution methods for inverse problems*, ed. D. Colton, H. Engl, A.K. Louis, J.R. McLaughlin, and W. Rundell, 147–54. New York: Springer-Verlag Wien.
59. Paltauf, G., J.A. Viator, S. A. Prahl, and S.L. Jacques. 2002. Iterative reconstruction algorithm for optoacoustic imaging. *J. Acoust. Soc. Am.* 112(4):1536–44.
60. Pan, X., Y. Zou, and M. Anastasio. 2003. Data redundancy and reduced-scan reconstruction in reflectivity tomography. *IEEE Trans. Image Processing* 12(7):784–95.
61. Anastasio, M., J. Zhang, X. Pan, Y. Zou, G. Ku, and L.V. Wang. 2005. Half-time image reconstruction in thermoacoustic tomography. *IEEE Trans. Med. Imaging* 24(2):199–210.
62. Zhang, J., M. Anastasio, X. Pan, and L.V. Wang. 2005. Weighted EM reconstruction algorithms for thermoacoustic imaging. *IEEE Trans. Med. Imaging* 24(6):817–20.
63. Anastasio, M., J. Zhang, E. Sidky, Y. Zou, D. Xia, and X. Pan. 2005. Feasibility of half-data reconstruction in 3-D reflectivity tomography with a spherical aperture. *IEEE Trans. Med. Imaging* 24(9):1100–12.
64. Pan, X., and M. Anastasio. 2002. On a limited-view reconstruction problem in diffraction tomography. *IEEE Trans. Med. Imaging* 21(4):413–16.